Postprint of: Szopińska M., Ryl J., Pierpaoli M., Closing the loop: Upcycling secondary waste materials into nanoarchitectured carbon composites for the electrochemical degradation of pharmaceuticals, CHEMOSPHERE Vol. 313 (2023), 137631, DOI: 10.1016/j.chemosphere.2022.137631

Closing the loop: upcycling secondary waste materials into nanoarchitectured carbon composites for the electrochemical degradation of pharmaceuticals

Małgorzata Szopińska[1], Jacek Ryl[2], Mattia Pierpaoli[3*]

[1] Gdansk University of Technology, Faculty of Civil and Environmental Engineering, Department of Environmental Engineering Technology, 11/12 Narutowicza St., Gdansk 80-233, Poland;

[2] Gdansk University of Technology, Institute of Nanotechnology and Materials Engineering, Division of Electrochemistry and Surface Physical Chemistry, 11/12 Narutowicza, Gdansk 80-233, Poland;

[3] Department of Metrology and Optoelectronics, Faculty of Electronics, Telecommunication and Informatics, Gdańsk University of Technology, Gdańsk, Poland.

Abstract

In this study, we demonstrated the application of electrochemical oxidation as a safer and cleaner technology for minimizing the impact of pharmaceuticals in wastewaters, simultaneously mediated by upcycled secondary waste materials (SWMs)-derived electrodes, to further reduce their environmental impact. The modularity, scalability, ease of operation and reliability make electrochemical oxidation an ideal process for the destruction of emerging persistent pollutants; however, their full-scale application is hindered by energy efficiency and the potential release of toxic by-products. Thus, the answer to these issues can be found in the design of tailored multifunctional electrode material. For the first time, SWMs derived from combustion and industrial processes have been employed with the simultaneous dual function of functional fillers, in a polyacrylonitrile fibrous matrix, and as a catalyst for the growth of carbon nanofeatures over the fiber surface, to increase the surface area and charge transfer. Next, the tailored composites were employed as anodes for the electrochemical oxidation of acetaminophen, both in phosphate buffer and in a real wastewater sample. The results suggest

* Corresponding author. Email: mattia.pierpaoli@pg.edu.pl
Department of Metrology and Optoelectronics, Faculty of Electronics, Telecommunication and Informatics, Gdańsk University of Technology, Gabriela Narutowicza 11/12, 80-233 Gdańsk (Poland).

that SWMs can substitute costly engineered fillers in carbon-based electrodes and that the absence of reaction by-products (monitored by UHPLC-ESI-MS/MS), together with the low energy consumption, make the tailored fibrous composite electrodes good candidates for the development of safer and cleaner technologies with reduced environmental impact.

Keywords

Advanced Oxidation Process; fly ash; spent foundry sand; chemical vapor deposition; carbon nanomaterial

1. Introduction

Utilization is one of the leading strategies for the management of hazardous industrial wastes such as fly ash (FA) and spent foundry sand (FS), thus, developing new pathways to minimize their environmental impact is currently a priority. Moreover, due to the ubiquitous presence and persistence of pharmaceuticals and recalcitrant pollutants in the environment, the development and implementation of efficient and cost-effective technologies to mineralize such treats are of primary interest.

FA is a particulate material produced from the controlled combustion of fuels, biomass or waste in thermal power plants and it constitutes a major concern for the environment, as it causes water, soil, and air pollution, and because of its costly disposal as a hazardous waste (Wang et al., 2019). For these reasons, diverting FA from landfills, where it also poses a significant threat to the environment, thus finding new pathways for its utilization from the perspective of the circular economy, also finds support in the European Commission guidelines (Gharfalkar et al., 2015). FS is a by-product resulting from the ferrous and nonferrous metal casting industries; it consists of high-quality silica particles, it has low absorption capacity, and it is non-plastic. The spent foundry sand is either recycled in non-foundry applications or landfilled. Indeed, the use of spent FS (originated only from iron, steel, and aluminum foundry operations) has found application in manufactured soils, soil-less potting media, roadway subbase, and as an aggregate for concrete production (Siddique and Singh, 2011), despite it potentially containing heavy metals, and hazardous organics, such as polycyclic aromatic

hydrocarbons (PAHs), benzene, toluene, xylene (BTEX), polychlorinated-p-dioxins (PCDDs), the related furans (PCDFs) and polychlorinated biphenyls (PCBs) (Environmental Protection Agency, 2014).

Acetaminophen (APAP) is the most widely available and prescribed analgesic and antipyretic pharmaceutical in the world, and its presence in the environment has started raising global concerns (Zhang et al., 2018) since it easily accumulates in the aquatic environment, and has been detected in surface waters, wastewater, and drinking water, and also because of its toxic metabolites and hazardous degradation by-products (Wu et al., 2012; Pacheco-Álvarez et al., 2022). While electrochemical oxidation has also been applied to the removal of APAP, the formation of intermediates such as hydroquinone, p-aminophenol, p-nitrophenol, and p-benzoquinone (Li et al., 2014; Zhang et al., 2022) has been reported, and these constitute a potential threat to the environment because of their toxicity and difficulty to degrade (Li et al., 2014; Al-Gharibi et al., 2021). For this reason, optimizing the degradation process, focusing on energy efficiency, and tuning the reaction pathway can be done by intelligently tailoring the material chemical structure and morphology at different scales.

Electrochemical oxidation is a reliable and effective water remediation technique for the mineralization of a plethora of water pollutants of current concern, among per- and polyfluoroalkyl substances (PFASs) (Pierpaoli et al., 2021c), pharmaceuticals, dyes and herbicides (Martínez-Huitle and Panizza, 2018; Brillas, 2021; Santos et al., 2021), even in complex and heavily concentrated matrices (Pierpaoli et al., 2021b). In our previous studies, we demonstrated how intelligently nanoarchitectured carbon hybrids possess superior efficiency in micro- and macro-pollutant degradation, due to both their morphology and chemical composition (Pierpaoli et al., 2021b), and that the chemical vapor deposition technique constitutes a preferential path toward the development of highly efficient, critical raw material (CRM)-free electrodes suitable for the designed process (Pierpaoli et al., 2020). Among different carbon allotropes, graphite electrodes are one of the most widely investigated electrode materials in the scientific literature, due to their low cost, availability, and non-toxicity; however, their effectiveness is limited due to their high corrosion rate at potentials higher than 1.7–1.9 versus SCE (Shestakova and Sillanpää, 2017). On the other hand, boron-

doped diamond electrodes (BDD) are known for their chemical and mechanical inertness, wide potential window, and ability to generate strong oxidants (Martínez-Huitle and Panizza, 2018), which makes them suitable for full-scale applications; however, commercially-available BDD are usually grown by CVD on CRM-containing substrates, such as Nb, with direct effect on the cost and sustainability. For this reason, alternative solutions charting a path towards greater sustainability and lower impact are a major issue. Graphene-based electrodes have only been developed in the last two decades, mostly by a bottom-up approach, being able to define a new class of electrode materials characterized by intermediate properties, and able to adsorb and degrade electrochemically a plethora of pollutants of emerging concern. Cui et al. fabricated a three-dimensional carbon brush using reduced graphene oxide through simple one-step electrodeposition and employed it as a cathode in a bio-electrochemical system for the removal of the azo compound (AO7) (Cui et al., 2018). They attributed the enhanced conductivity and increased electrochemical surface area to the improved AO7 removal efficiency. Similarly, Ormeno-Cano and Radjenovic realized porous boron and nitrogen-doped graphene-based sponge electrodes for the electrodegradation of selected antibiotics, attributing plane the enhanced removal to the strong π-π interactions between the antibiotics and the graphene basal (Ormeno-Cano and Radjenovic, 2022). The inclusion of different nano- and micro-fillers into carbon fibers is generally beneficial to enhancing the mechanical and electrical properties, both inherited by the filler itself and due to their intrinsic catalytic properties. Indeed, Rajabpour and coworkers demonstrated how a graphene sheet can act as a seed to expedite the alignment of all-carbon rings and can be responsible for enhancement of the mechanical properties (Rajabpour et al., 2021).

For these reasons, in this study, novel carbon mesostructured electrodes were synthesized for the first time by a simple phase inversion technique combined with a single carbonization-surface decoration step performed in a CVD reactor. Hazardous secondary materials (HSMs) were incorporated into the electrode bulk with the aim of both reducing their environmental impact, by diverting them from landfilling, and acting as catalysts for the development of nano/micro-sized carbon structures on the electrode surface. A comparison with commercially-available graphene oxide flakes and diamonds fillers was also performed.

Finally, the acetaminophen degradation efficiency was evaluated for the different architectured electrodes, both in phosphate buffer solution and in a real treated wastewater effluent, aiming to simulate their utilization as an advanced tertiary treatment.

2. Materials and methods

2.1 Materials

Polyacrylonitrile (PAN) and APAP (purity >98%) were purchased from Merck. Dimethylformamide (DMF, pure p.a) was bought from POCH (Poland). Phosphate buffer solution (PBS, 0.1 M) was prepared as described in our previous work (Pierpaoli et al., 2021a). Pharmaceutical standard (analytical standard grade) acetaminophen was purchased from Sigma-Aldrich (USA). A stock solution of 500mgL^{-1} and a working solution of 100mgL^{-1} for method calibration were prepared in LC-MS grade methanol (Optima, Fisher Scientific) and stored at -20 °C. Acetonitrile (ACN, LC-MS grade Optima) and formic acid (98–100%, LiChropur for LC-MS) were purchased from Fisher Scientific and Sigma-Aldrich (USA), respectively. Purified water (ultrapure water, resistivity 18.2 MΩ cm at 25 °C) was obtained via a Direct-Q® Water Purification System. The composition of the treated wastewater (TWW) was analyzed using the methods described in our previous work (Pierpaoli et al., 2021c).

Table 1 – Treated wastewater characteristics [mean±standard deviation]

	Parameter	Value
Organic matter characteristics	COD [mg L^{-1}]	34.0±2.1
	BOD_{20} [mg L^{-1}]	<LOD
	TSS [mg L^{-1}]	3.2±0.1
	MSS [mg L^{-1}]	1.6±0.1
	VSS [mg L^{-1}]	1.6±0.1
Nitrogen forms	N-NH_4^+ [mg L^{-1}]	0.103±0.015
	N-NO_3^- [mg L^{-1}]	4.69±0.50
	N-NO_2^- [mg L^{-1}]	6.11±0.61
	TN [mg L^{-1}]	10.10±0.81
Phosphate forms	P-PO_4^{3-} [mg L^{-1}]	0.62±0.25
	TP [mg L^{-1}]	0.768±0.016
Other ions	Cl^- [mg L^{-1}]	86.6±2.1
	SO_4^{2-} [mg L^{-1}]	37.9±1.8

	S^{2-} [mg L^{-1}]	<0.1
Basic physicochemical parameters	pH	8.37±0.10
	redox [mV]	187.8±9.8
	Conductivity [mS cm^{-1}]	1164±2.2
Selected micropollutants	APAP [µg L^{-1}]	<LOD

Abbreviations: COD – chemical oxygen demand, BOD – biological oxygen demand, TSS – total suspended solids, MSS – mineral suspended solids, VSS – volatile suspended solids, TN – total nitrogen, TP – total phosphorus, LOD – limit of detection

2.2 Creation and characterization of polymeric electrodes

A solution of 10%w PAN in DMF was prepared and stirred for 24 hours, then a selected filler (Table 2) was added into the mixture and vigorously stirred by a vibration shaker (Vibration stirrer ZX4 Vortex Mixer Velp) until a homogenous solution was obtained.

Table 2 – Description of the fillers used in bulk in the composite realization

Filler name	Filler type	Filler description	Filler dimensions
ND	Diamonds suspension	Commercially available micro-sized diamond suspension	0.6–1.3 µm
GO	Commercial graphene oxide	Commercially available flat graphene oxide flakes	0.2–2.8 µm
FA	Biomass fly ash	Fly ash from a biomass source, obtained from an oxidating atmosphere process	1.7–3.0 µm > 7.5 µm
FS	Foundry sand waste	Foundry sand used in a casting process at a temperature of up to 1400 °C	60–140 nm 140–830 nm > 5 µm

In the case of ND, firstly, a dispersion of ND in dimethylformamide (DMF) was prepared by repeatedly centrifuging and replacing the original solvent (dimethylsulfoxide, DMSO) and finally sonicating. Due to the poor dispersion stability, the PAN was directly added to the ND/DMF solution and vigorously stirred until the polymer extruded in a water-based coagulation bath. Composite electrodes were obtained by the wet-spinning method, using an in-lab made apparatus, then compressed into cylinder electrodes, stabilized, and carbonized by CVD. The detailed procedure can be found in our previous work (Pierpaoli et al., 2022). Simultaneous carbonization and nanofeatures growth were performed by a microwave plasma-

assisted chemical vapor deposition (MWPECVD) system (SEKI Technotron AX5400S, Japan). During the CVD process, which lasted for 40 minutes, the microwave power and the total pressure were kept at 1100 W and 40 Torr, respectively. The substrate holder temperature was set at 550 °C. A gas mixture of H_2, CH_4, and B_2H_6, with a total flow of 328 sccm, was used for the BDD growth. After the fiber wet-spinning procedure and stabilization process in cilindrical mold, flattened cylindric-shaped electrodes, having diameter of 9.45mm (SD=1.0mm) and thickness of 2.0mm (SD=0.17mm) are produced, for a total area of approximately 2 cm^2 (1.96 ± 0.42 cm^2). After carbonization/CVD-growth process, different shrinkage occurs dependently on the filler employed, resulting in a decrease of the electrode geometrical area (ranging between 30% for the only PAN to 7% for the FA) but in an increase of the total exposed one. Scanning electron microscopy (SEM) imaging was carried out using an FEI Quanta 250 FEG (ThermoFisher Scientific) equipped with a Schottky field emission gun and operating with secondary electrons under a 20 kV accelerating voltage. X-ray Photoelectron Spectroscopy (XPS) analyses were done with an Escalab 250Xi (ThermoFisher Scientific) multispectroscope. The spectroscope was operating with an AlKα X-ray source and a spot diameter of 650 μm. The pass energy through the hemispherical analyzer was set to 20 eV. The charge compensation was guaranteed by a low-energy electron and low-energy Ar^+ ion flow, with a final peak calibration at adventitious C 1s at 284.6 eV. Raman spectra were acquired using a commercial Raman microscope (LabRam Aramis, Horiba) on excitation by a 632.8 nm HeNe laser with up to 20 mW optical power at the sample. An integration time of 5 s (20 averages) with a diffraction grating of 300 lines per mm was set, using a 50x magnification objective. All of the peaks were fitted with Lorentzian functions after the spectra were baseline subtracted. Peak ratios were calculated by considering their area, instead of intensity, due to the heterogeneity of the composite material. An Inductively Coupled Plasma – Optical Emission Spectroscopy (ICP-OES) analysis was carried out to assess the presence of metals in trace quantities from the SWMs after performing an acid (HNO_3/HCl 1:3 solution) digestion procedure. The electrochemical properties of the electrode were measured by a VMP-300 BioLogic potentiostat, in a three-electrode cell configuration, in which the BDD, a platinum wire, and an Ag/AgCl 3M KCl electrode were used, respectively, as the working, counter and reference

electrodes in PBS 1M as the electrolyte. The EIS experimental data was fitted using the BioLogic EC-lab software.

2.3 Electrochemical oxidation setup

Electrochemical oxidation batch tests were performed in a completely stirred borosilicate beaker as reactor, with an initial volume of 35 mL, in which the electrode sample is completely immersed (Fig. S1). Twenty minutes after the APAP solution was added to the reactor, to distinguish the adsorption phase from the oxidative, a 2 mL sample was taken from the beaker and a constant voltage of +3 V was applied to the electrode. At 5, 15, 30, and 60 minutes, samples having a volume of 1 mL each were taken and directed to an ultra-high performance liquid chromatography tandem mass spectrometry with electrospray ionization (UHPLC-ESI-MS/MS) analysis. The current density was measured during the process. Chemical analyses of the APAP were performed by UHPLC-ESI-MS/MS (UHPLC Nexera XR coupled with LC/MS-8050, Shimadzu Company) using an external calibration method. Shim-pack SP-C18, 2.1 x 150 mm, and 2.7 µm was used as an analytical column. A gradient flow was applied starting at 0.15 $mlmin^{-1}$, ramped up to 0.25 $mlmin^{-1}$ over 4 min, kept at this level until the 9.5 min mark, then returned to 0.15 ml (11 min), and maintained here until the 12 min mark. A gradient mobile phase was used; starting at 95% mobile phase A (0.3 % formic acid in ultrapure water, and 5% of mobile phase B (1:1 MeOH, ACN, solution) kept until the 4 min mark, followed by a linear increase over 8 min to 65% A and 35% B, a second increase to 100 % B at the 9 min mark, maintained until 9.5 mins. (washing stage), then returned to the initial conditions (11 min mark), and held for 1 min (re-equilibration to initial condition). The column temperature was maintained at 40 °C and the autosampler at 4 °C. The total run time was 12 min. LC eluate was sprayed into a tandem mass spectrometer by electrospray ionization in the positive ion mode. The interface setup parameters were as follows: nebulizing gas flow (N2, 2 Lmin-1), heating gas flow (N2, 8 $Lmin^{-1}$), interface temperature (150 °C), desolvation temperature (261 °C), heat block temperature (400 °C). The APAP eluted at 6.75±0.05 min and was a monitored by multiple reaction monitoring (MRM) transition m/z 152.0 > 110.2 (collision energy (-17 eV); quantifier transition) and m/z 152.0 > 65.2 (collision energy (-29 eV); qualifier transition).

Potential APAP oxidation products include hydroquinone (ESI+, MS m/z=123), p-benzoquinone (ESI+, MS m/z=121), ketomalonic acid (ESI+, MS m/z=119), maleic acid (ESI+, MS m/z=117), oxalic acid (ESI+, MS m/z=91), oxamic acid (ESI+, MS m/z=90), and acetamide (ESI+, MS m/z=60), and were evaluated using scanning single ion monitoring mode (SIM) under the same chromatographic conditions after Li et al. (Li et al., 2014). The sample injection volume was 1 µL. The calibration curve was plotted using 5-level calibration (linearity 1–1000 μgL^{-1}. The method detection limit (MDL) and method quantification limit (MQL) were 1 and 3 μgL^{-1} and 1.5 and 4.5 μgL^{-1} for water and wastewater matrix, respectively. For this method, no analyte pre-concentration was applied. To evaluate the APAP removal efficiency as function of the energy consumed, the specific electrical charge (Q) is reported as follow: Q=Jt/V where Jt is the integral of the measured current over time (A*h) and V is the solution volume (L) (Anglada et al., 2009). Since the applied potential is constant, Q is directly proportional to the power used.

3. Results and discussion

3.1 Electrode characterization

Due to their nature as combustion products, FA and FS do not possess a well-defined morphology and chemical composition, but they are rather dependent on the combustion process parameters and feedstock composition. For this reason, a more in-depth analysis was performed to characterize the waste materials. From Fig. 1a, it is possible to observe the presence of both spherical and irregularly shaped particles.

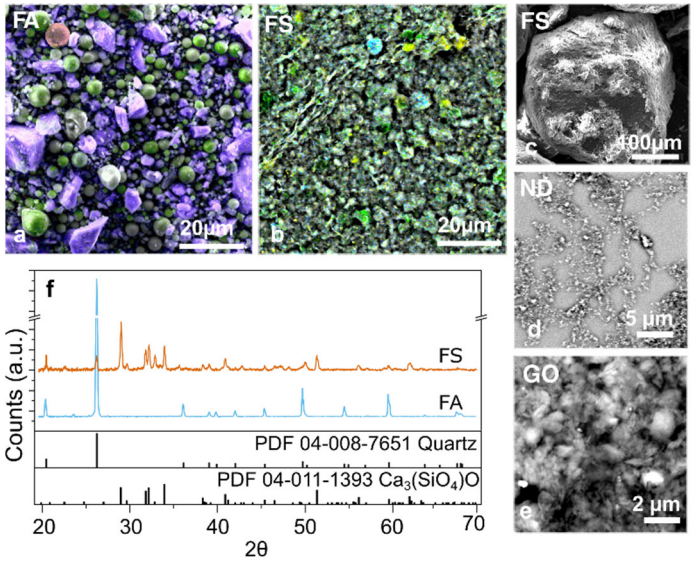

Fig. 1 – SEM-EDX pictures of (a) FA (in yellow aluminum silicates, in blue calcium silicates and in red Fe-rich particles; (b) fine fraction of FS (in green calcium carbonates, in yellow calcium silicates and in blue Fe-rich) and (c) large fraction of FS. SEM of (d) ND solution dried on Si substrate; (e) GO flakes, and XRD diffractograms of FS and FA. The reader is referred to the web version of this paper for the color representation of this figure.

In particular, a bimodal particle size distribution is present in the FA sample, with the smaller fraction accounting for particles having a diameter between 1 and 3 μm and the larger one having an equivalent diameter larger than 8 μm. FS is mostly constituted by subangular sand with obtuse angles, with a diameter ranging from tens to hundreds of micrometers (Fig. 1c) and a superfine fraction (0.05–1 μm, Fig. 1b), which results from the presence of inorganic and organic binders, and other additives used during the casting process (Siddique and Singh, 2011). Quartz and calcium silicate are the prevalent crystalline form (Fig. 1e); however, Al is predominant as well, as determined by the EDX analysis, and other elements are present in minor quantities, as reported in Table S1. Indeed, a major difference arises between FA and FS, related to the Fe content, especially after acid treatment, suggesting a different composition (Table S2). The commercial ND suspension presents particles agglomerating into larger structures (Fig. 1d), as well as for the graphene oxide flakes (Fig. 1e).

GO, NDs, FA and FS were then added to the PAN/DMF solution, and the electrodes were

synthesized. SEM images of the different electrode composites, after CVD-carbonization, are reported in Fig. 2.

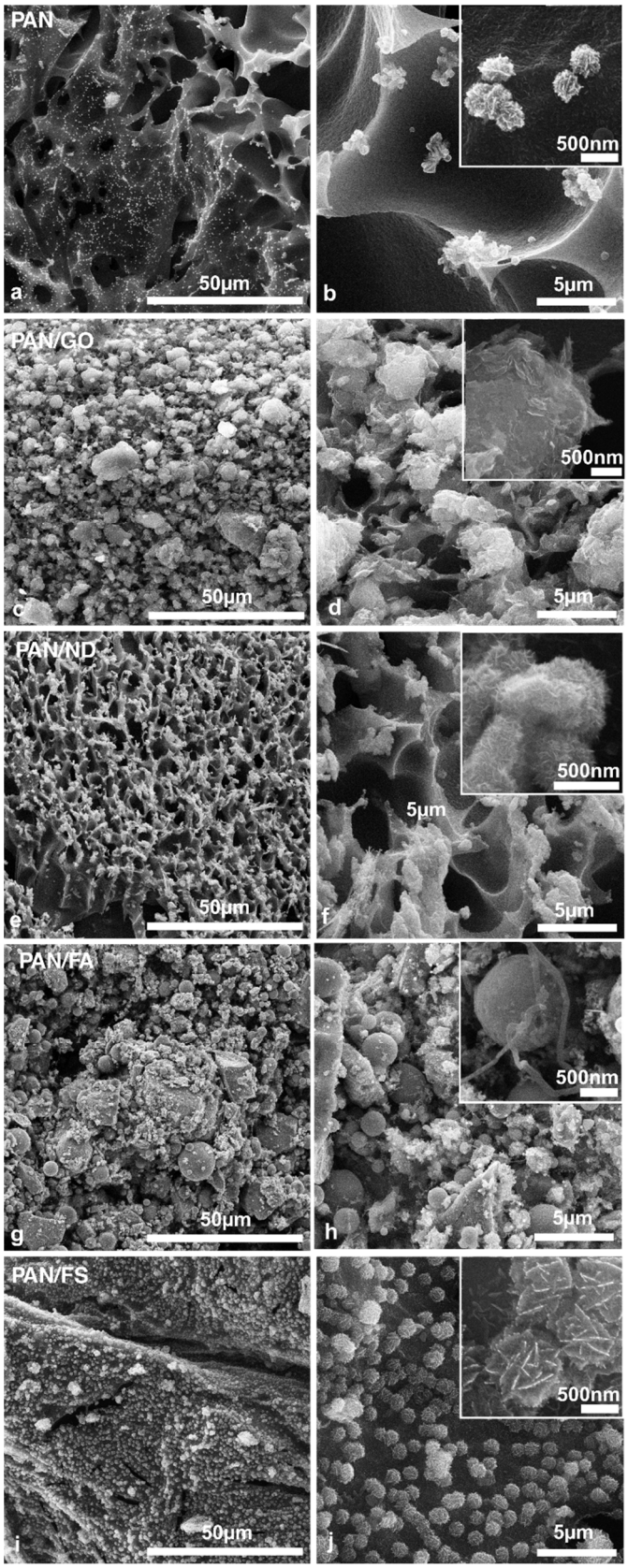

Fig. 2 – SEM of the differently synthesized composite materials before the oxidation tests.

It is possible to observe the characteristic fiber morphology in Fig. 2a, obtained by the combined action of phase inversion during the wet-spinning process, and the effect of the plasma in etching the outer fiber interfacial layer. A few micrometer-sized carbon nanowalls-flakes are present on the pores' edges as a result of the locally-enhanced plasma during CVD (Fig. 2f). The addition of different powders dramatically affects the composite morphology. For both GO and NDs, it is still possible to observe a similar porous structure, which is more open for the PAN/ND composite, while it is partially clogged by the GO flakes in the case of PAN/GO (Fig. 2g), where it is possible to observe the presence of the wrinkled graphene sheets on the composite surface. Indeed, the GO flakes hinder the transport of ionic species toward the PAN microporous structure, as also demonstrated by the electrochemical characterization, in Fig. 3. The presence of NDs leads to the formation of a highly developed agglomerated structure during the CVD process constituted by tiny carbon nanowalls (Fig. 2h). The presence of different carbon architectures in the PAN/FA composite is the result of the FA chemical heterogeneity. In particular, it is possible to observe both amorphous carbon and the formation of fibers and nanotubes, catalyzed by the presence of Fe within FA (Fig. 2i). Nevertheless, in the PAN/FS composite, most of the larger particles have sedimented in the spinning solution, thus only the finer FS fraction is present in the composite; moreover, it is interesting to observe the formation and a high density of nanowall-coated spherical structures which cover most of the fiber surface, with a very limited porosity (Fig. 2j).

The electrochemical behaviors of the different carbon electrodes were systematically tested in-situ, using the same reactor for the APAP EO tests. Fig. 3a–e reports the voltammograms at different scan rates for all five of the composites in 1M PBS, at a potential window from 0 to 0.4 V. The CV curves of bare PAN, PAN/ND, and PAN/FS composites present the characteristic shape of an electrochemical double-layer capacitor (EDL). The large rectangular-shaped area for these two composites suggests better electrolyte penetration in the pores compared to the PAN/GO and PAN/FA. Indeed, in the later ones, at high scan rates, an oval-shaped resistive-capacitive behavior is observed, which is related to a high instability of EDL and the poor capacitive nature of the electrodes. The main factor affecting ionic diffusion within the porous structure of carbon materials is the structure of the porous network itself. By plotting current

versus the scan rate, straight interpolating lines were obtained, to estimate the EDL capacitance values (Fig. S2).

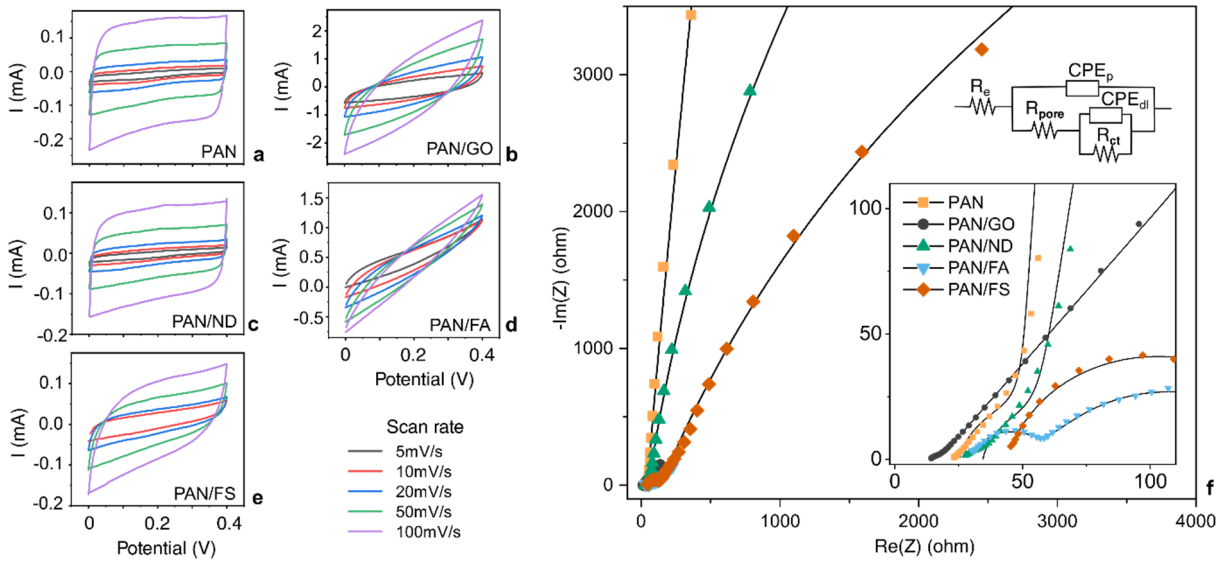

Fig. 3 – (a–e) Cyclic voltammograms at different scan rates for all 5 composites in 1M PBS, at a potential window from 0 to 0.4 V. (f) EIS Nyquist plot. Straight lines are results of EEC fit. The reader is referred to the web version of this paper for the color representation of this figure.

To further examine the interfacial charge transport dynamics of the synthesized composite electrodes, electrochemical impedance spectroscopy (EIS) was employed. Fig. 3f shows the Nyquist plots, highlighting the different behaviors across the 200 kHz – 20 mHz frequency range. The obtained semicircles were fitted with an equivalent electrical circuit (EEC) model, reported in the inset, which includes the solution resistance (R_s), pore resistance (R_p), pore capacitance (CPE_p), charge transfer resistance (R_{ct}), and double-layer capacitance (CPE_{dl}); the fitted parameters are tabulated in Table S4. Unexpectedly, despite the different origin and chemical composition of the powders, their incorporation within the PAN composite was found to have a minor effect on the conductivity of the electrode, as described by the comparable value of R_s, equal to 30±15 Ω. The reason for such a finding may be that the CVD-growth electrode surface constitutes the preferential path for the charge transfer rather than the fiber bulk. Indeed, the lowest R_s belongs to the PAN/GO, for which stacks of GO flakes are recognizable from the SEM picture (Fig. 2g). Similarly, the first semicircle in high-frequency

regions is easily distinguishable for all of the samples, which is attributed to the combined effect of charge transport resistances at the electrode/electrolyte interfaces (R_{ct}). At a first look, PAN, PAN/ND, and PAN/FS exhibit similar behavior and they fit the EEC well, characterized by a large semicircle at low frequencies related to the bulk Nernst diffusion. However, examining the different Nyquist plots individually, the smaller semicircle at high frequencies indicates a faster ionic transference within the EDL for the PAN/GO sample, followed by a linear response in the low-frequency region, resulting in an angle of 45° with the axis, which corresponds to low ionic diffusion resistance (well-represented by a Warburg element (Randles, 1947). EDL capacitance values obtained from CV and EIS studies were compared and used to estimate the electrochemical surface area (ECSA), since this method allows for accounting the total surface accessible to the solution. ECSA was estimated utilizing the relationship ECSA = C_{dl} / C_S, where C_S is the specific capacitance of the investigated material. However, the exact C_S value is typically unknown, leading to substantial errors in ECSA determination from CDL. It is commonly accepted to use a single C_S value for ECSA for comparative purposes, yet the numbers obtained this way may be under- or overestimated (Morales and Risch, 2021; de Freitas Araújo et al., 2022). For comparison, we considered 0.06 mF cm^{-2} based on the previous literature reports for porous carbonaceous materials (de Freitas Araújo et al., 2022). The estimated ECSA it is between 16 cm^2 for PAN and ND and almost double for FA and FS (22 and 34 cm^2 respectively), while for GO is 150 cm^2, which could be overestimated.

The Raman spectra presented in Fig. 4a show the difference between the different composites, before and after the EO tests. The spectra were deconvoluted and the peak was analyzed, by considering bands at 1577 (9), 1337 (6), 1612 (8), 1493 (12), and 1189 (12) cm^{-1} (standard deviation in brackets), attributed to the G (graphitic, attributed to E_{2g} phonon vibrations of sp^2 carbon atoms), D (corresponding to the A_{1g} breathing mode, attributed to the disorder-induced defects), D' (appearing as a shoulder of the G peak, observed in microcrystalline graphite and glassy carbon), D* (a broad band, attributed to amorphous carbon and to the presence of hetero-atoms as impurities in the carbon lattice) and D" (trans-polyacetylene) bands (Lee et al., 2022).

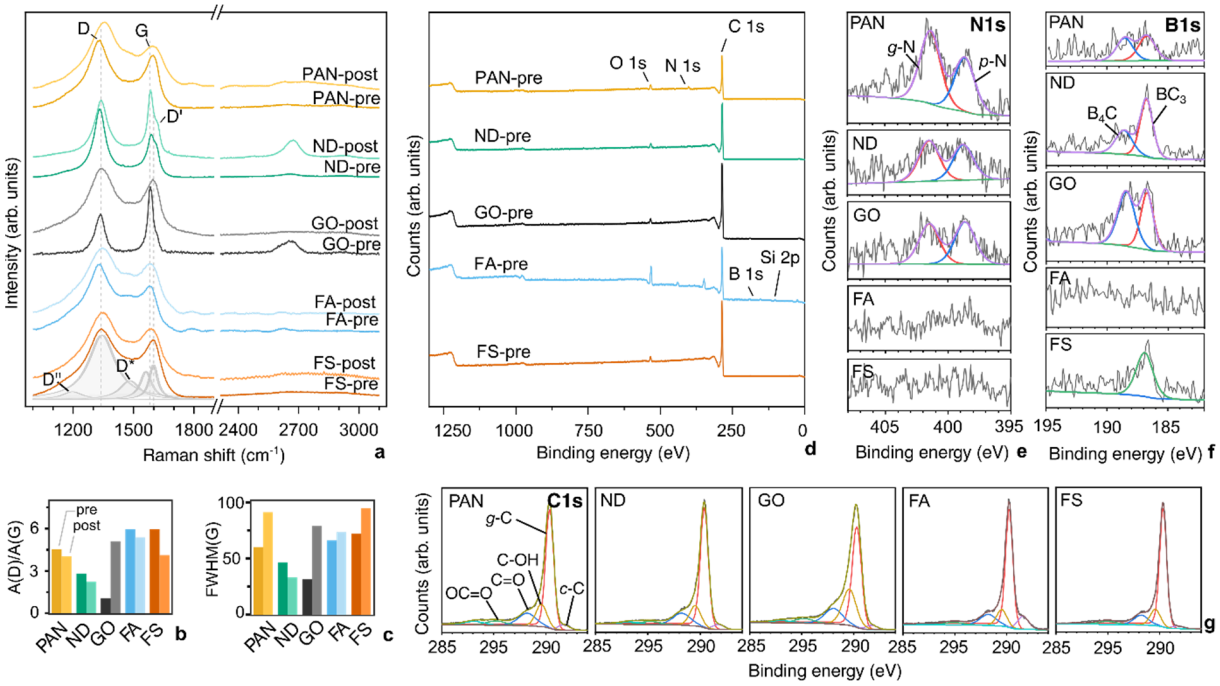

326

327 *Fig. 4 – (a) Raman spectra, with an example of the peaks used for the deconvolution, (b) A(D)/A(G)*

328 *ratios, (c) FWHM(G) of the samples before and after EO tests. (d) A(D)/A(G) versus ratio*

329 *A(D')/A(G). X-ray photoelectron spectroscopy (XPS) spectra of the different samples: (d) survey*

330 *spectra; (e) N 1s spectra; (f) B 1s spectra; and (g) C 1s spectra. The reader is referred to the web*

331 *version of this paper for the color representation of this figure.*

332 The position, intensity (relative to the G-band, expressed as a ratio) and broadening of the D
333 band depends on the type of disorder, the presence of impurities, and functional groups. The
334 intensity ratio of A(D)/A(G) is commonly used as an estimator of the defect density in carbon
335 materials since it is sensitive only to defects in the rings. In particular, the relative peak
336 intensity, expressed as the ratio of the integrated area of the D and D′ bands, has been preferred
337 because the area under the band represents the probability of the whole scattering process
338 (Martins Ferreira et al., 2010; Del Corro et al., 2014). Firstly, by comparing the A(D)/A(G) of
339 the different composites, before EO, it is possible to observe that the ratio is lower for the
340 composites containing ND and GO. Thus, the presence of such engineered carbon nanofillers
341 may improve the formation of a large ladder structure, being converted into a large graphene
342 layer. All of the samples, with the exception of the PAN-GO, show a slight decrease in the
343 A(D)/A(G) ratios after the EO tests (Fig. 4b and Table S4), which can probably be attributed to

the oxidation and elimination of amorphous and disordered carbons, leaving exposed the better-crystallized fiber surface, as also supported by their FWHM(G). It is interesting to observe that the biggest difference belongs to the PAN/GO sample, already visible by qualitatively comparing the spectra (Fig. 4a). In contrast, the A(D)/A(G) ratio for the PAN/ND sample after EO is significantly lower than the others. On the other hand, the FWHM of the G peak always increases for the increasing disorder, since this parameter is sensitive to all types of defects, either in the sp^2 rings or chains (Eckmann et al., 2013), making it a good indicator of the degree of graphitization of carbonaceous materials. Thus, the widening of the D and G peaks after the EO process (Fig. 4c) was also observed in our previous studies (Pierpaoli et al., 2021b) for sp^2-C-rich carbon nanoarchitectured electrodes, while almost no difference was found for boron-doped diamond ones. Indeed, it is interesting to find that the PAN-ND composite belongs to the lowest FWHM, probably due to the beneficial effect of NDs within the structure of the fiber acting as nucleation seeds, in a similar fashion as reported by (Rajabpour et al., 2021).

Furthermore, XPS was performed on CVD-carbonized PAN composites to quantify the differently hybridized carbon and functional groups. XPS survey spectra are shown in Fig. 4d. The N1s XPS spectra were deconvoluted into two peaks: at around 398.7 eV, attributed to pyridinic N, and at around 401.5 eV, corresponding to graphitic N. The presence of the pyrrolic N peak can overlap the graphitic N; however, due to the low N content (< 4%), it is difficult to distinguish the peaks, especially for the PAN-FA and PAN-FS composites, for which a higher amount of fillers is present. Thus, it is possible to affirm that the nitrogen is related to the bare PAN structure, differently from the boron which is associated with the nanostructure growth, due to the introduction of B_2H_6 during the MPECVD process. Indeed, it is also possible to qualitatively compare the grown nanostructure by the SEM reported in Fig. 2, with the presence of the B1s profiles. The B1s profiles shown in Fig. 4f indicate that several B species are present and incorporated within the CVD-grown nanostructure, and the two peaks, at approximately 188.6 and 186.8 eV, could correspond to B_4C and BC_3, respectively (Bepete et al., 2013). The BN peak is not present (191 eV), due to the low N content, limited to the PAN fiber, and not available as a gas precursor, while the presence of B_4C is inhibited in the PAN-

FS composite. Finally, the C1s spectra (Fig. 4g) show five peaks after deconvolution. The peak at 284.7 eV corresponds to graphitic carbon. The peak at 283.3 eV can be associated with the carbidic components (SiC, BC) for the PAN/FS and PAN/FA composites. The peak at 285.4 eV is likely to arise from the graphene domain edges and defects, or by C-OH. The higher binding energy peaks at ca. 286.8 and 289.9 eV are attributed to the formation of C–O bonds. For a quantitave comparison, fitted results of C1s, N1s and B1s core level XPS spectra for the different composite electrodes are reported in Table S5.

3.2 Electrochemical oxidation tests

The oxidation of organic compounds by electrochemical technique involves two different mechanisms acting simultaneously: direct anodic and indirect oxidations. In the first, the electron transfer between the organic compound and the anode occurs directly on its surface, while in the indirect oxidation, the electrochemical process is mediated by highly reactive oxidant generated by the reaction with other species (e.g. hydroxyl radical, chlorine active species), which are electro-generated at the anode surface (Martínez-Huitle and Panizza, 2018; Wilk et al., 2022). Moreover, secondary oxidants reactive sulfate species (sulfate radicals, peroxydisulfates) at appropriate current density may also occurs during EO (Ganiyu et al., 2021). Possibility of their in-situ EO generation, especially in sulphate-reach matrix constitute additional influence for effective degrading organic contaminants. Indeed, $S_2O_8^{2-}$ can be electrosynthesized from the SO_4^{2-} oxidation, resulting, then, in the cathodic production of $SO_4^{\bullet-}$ (Araújo et al., 2022) also by sp2-C rich boron-doped diamond hybrid electrodes (de Freitas Araújo et al., 2022). However, considering the relatively low concentrations of chloride and sulphate ions in the studied matrix (Table 1), the contribution of such electrogenerated oxidants, may play a minor role in the mineralization process. However, the anode material plays a predominant role in favoring one or other pathway (Brito et al., 2021). In particular, the higher charger transferability, the larger active surface, and superior stability are preferential for ideal electrode material (Faber et al., 2014). Indeed, it has been reported that B, N co-doping reduces the charge transfer resistance, induces high electrical conductivity, and fosters quicker EOP kinetics (Zhang et al., 2020).

To oxidize APAP on gassy carbon electrodes, a potential ranging between 0.2 and 0.7 V vs SCE should be applied to the anode, depending on the solution's pH, as has been reported (Nematollahi et al., 2009). However, a higher applied potential may be necessary to directly transfer electrons from the APAP to the anode, and to allow the formation of different oxidants. Moreover, the APAP oxidation pathway is known to follow complex kinetics, due to the variable OH concentration caused by the parallel consumption of this oxidant in fast reactions with products (Brillas et al., 2005). The electrochemical degradations of APAP were evaluated both in phosphate buffer (PB) and treated wastewater (TWW) by the different composite electrodes.

3.2.1 EO in phosphate buffer

Degradation of APAP was quantified as a pseudo-first-order kinetic in PBS (Fig. 5a) and a pseudo-zero-order kinetic in TWW (Fig. 5e), under the application of a +3V vs Ag/AgCL 3M KCl electrode. The initial concentration of APAP was set as 10 mg/L for all of the reported experiments, in a 0.1M PBS. Before the application of a constant potential to the electrode, the solution was stirred with the PAN-based electrode composite and allowed to rest for 20 minutes to allow adsorption (Fig. 5c). The presence of a high level of graphitization on the carbon surface seems to play an important role in adsorption, allowing for the π–π interaction with the benzene ring present in the organic molecules (Tian et al., 2020). As can be observed in Fig. 2i, the PAN/FA morphology lacks a porous carbon-rich coating, while it catalyzes the growth of nanofiber-like structures, thus exhibiting the lowest adsorption. To compare the APAP removal efficiencies with the energy consumed, Fig. 5b reports the plot between the efficiency and specific current density, measured during the tests. It is possible to observe that, while the PAN-GO electrode exhibits the faster removal kinetic (Fig. 5a), it also has the highest energy consumption, since part of the energy is consumed by the electrode oxidation, as is also well documented by the big difference in the Raman spectra before and after the EO process (Fig. 4a). For this reason, it was deemed appropriate to compare the angular coefficients of the linear regressions, which express the APAP oxidation efficiency at a specific energy density (Fig. 5b), which have been reported in Fig. 5d. The APAP adsorption, evaluated at the beginning of the tests (Fig. 5c) shows a comparable effect between the different composites,

except for the PAN/FA sample, which does not show an outer carbon “skin” at the solid/liquid interface, which can be simply explained by the low π–π interactions.

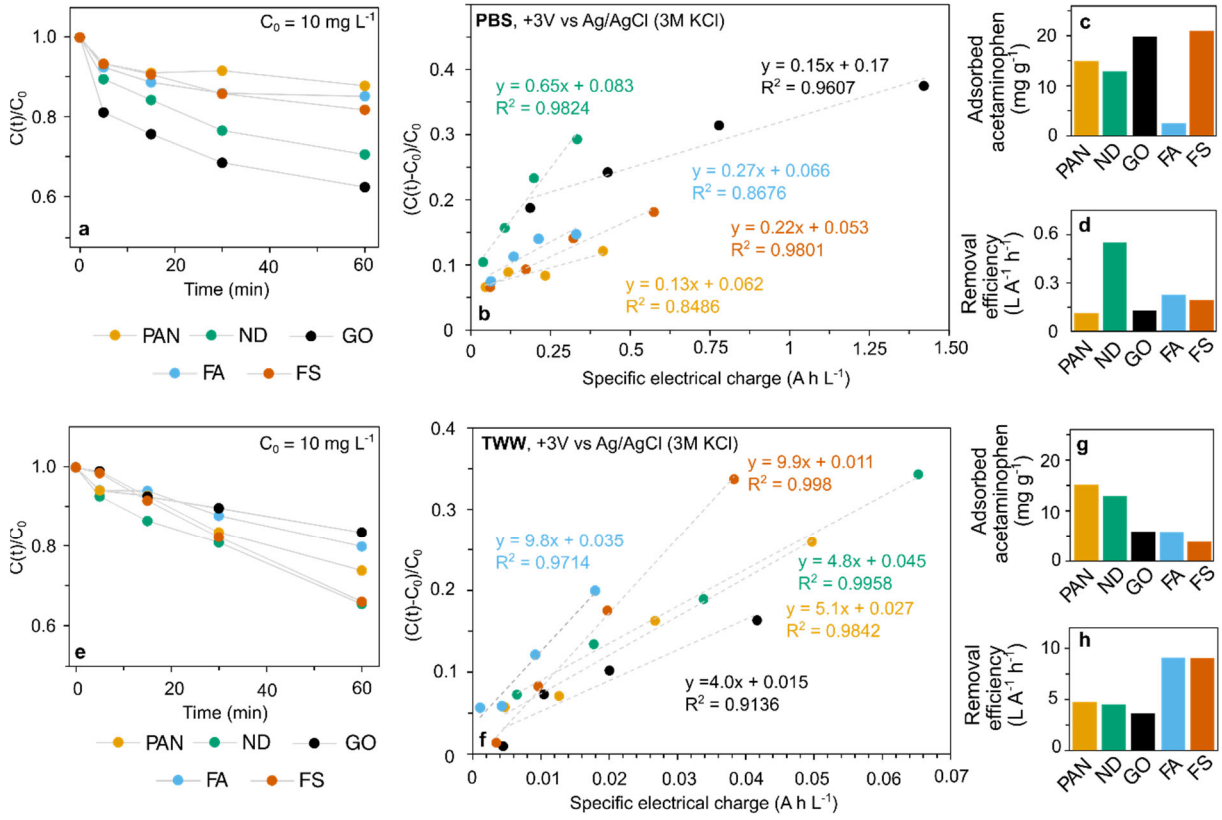

Fig. 5 – (a,e) normalized APAP concentration versus time. (b,f) comparison between APAP removed and specific energy density measured. (c,g) APAP initially adsorbed by the electrode and (d,h) their corresponding removal efficiency in 0.1M PBS at the applied potential of 3 V vs AgAgCl 3KCl. The reader is referred to the web version of this paper for the color representation of this figure.

We also further investigated the impact of chloride species on the AC degradation, (PBS containing 0.137 M NaCl, 2.7 mM KCl, 8 mM Na_2HPO_4, 2 mM KH_2PO_4) on the degradation of AC, finding that more than 99% was degraded in the first 5 minutes, for all of the electrodes. The redox chemistry of aqueous chlorine species depends on several experimental conditions, such as the solution pH, which results in the different fractioning of different aqueous active chlorine species. Indeed, during the electrochemical oxidation process, Cl- could be oxidized to Cl_2, Cl_2O, or HClO, all of which indirectly participate in the APAP oxidation reactions (Wilk et al., 2022), thus explaining the abrupt APAP degradation.

3.2.2 EO in TWW

To assess the effectiveness of employing the synthesized electrodes for the electrochemical degradation of pharmaceuticals in relevant environments as an advanced treatment, the oxidation of APAP, as a representative widespread drug, from a real TWW matrix was investigated. Firstly, TWW is characterized by a lower conductivity than PBS, which implies an increase in the applied potential for the same current density. On the other hand, the higher potential may result in the formation of different active species that may participate both in the indirect oxidation processes, oxygen evolution, and accelerated electrode degradation; thus, it was decided to apply the same potential, with the result of a lower current density on the electrode, thus a reduced removal efficiency. Similar behaviors were observed in other studies, such as in tap water, due to the lower conductivity (Ormeno-Cano and Radjenovic, 2022) and the absence of organic matter (Pierpaoli et al., 2021c). It is worth reporting that the PAN/ND composite exhibits a higher removal efficiency in PBS (Fig. 5d). BDD electrodes are known to possess a distinct advantage over other electrode materials of their stability, chemical inertness, due to the C atoms in sp^3 hybridization (Martínez-Huitle and Panizza, 2018). Even if their presence was not directly probed on the PAN/ND surface, their presence in the PAN bulk may induce a less defective structure (Fig. 4), therefore resulting in a wider active surface, not limited to the single BDD grain boundaries exposed to the electrolyte. The highest efficiencies attributable to FA and FS (Fig. 5h) may also be attributable to their lower capacitive behavior (Table S4), favoring faradaic processes instead. For both tests, pH increases with time, more remarkably in TWW (from 7.7 to 10.5 after 1h of treatment), rather than PBS (from 7.8 to 8.0).

In summary, both the electrode morphology and the chemical structures play important roles in the APAP degradation: Zhang et al. reported that co-doped atoms and the unsaturated carbon atoms provide a series of potential active sites; in particular, the copresence of B, carrying negative charges due to the strong electronegativity, with C neighboring atoms, represent a preferential site for the adsorption of O and O_2 intermediates (Zhang et al., 2020). Interestingly, no by-products, inc. hydroquinone, p-benzoquinone, ketomalonic acid, maleic acid, oxalic acid, oxamic acid, and acetamide, were identified during the EO processes (Fig. S3,

S4).

4. Conclusion

In this study, we demonstrated how to upcycle hazardous waste into architectured electroactive carbon-based electrodes and demonstrated their potential for the oxidation of acetaminophen, as a putative pharmaceutical, in real wastewater. Combustion by-products and industrial waste can be used as inexpensive fillers in polyacrylonitrile-based composites and as catalysts, able to induce the growth of different carbon nanostructures by catalytic chemical vapor deposition. The introduction of fly-ashes and foundry sand waste into the PAN matrix resulted in an acetaminophen electrochemical removal efficiency twice that of the bare PAN-based electrode, which acts differently as a catalyst during the CVD process: while large the Fe-rich particles in the FA catalyze the formation of tubular carbon nanostructures, the complex sub-micron FS fraction enhances the degree of graphitization of the composite electrode. The addition of nanodiamonds, acting as a nucleation seed, positively affect the CVD-grown interfacial structure, resulting in a more ordered graphitic structure, which is related to the fastest degradation kinetics, both in PBS and TWW. On the other hand, the addition of graphene oxide into the electrode is detrimental, since most of the energy is consumed in the electrode oxidation. No by-products, inc. hydroquinone, p-benzoquinone, ketomalonic acid, maleic acid, oxalic acid, oxamic acid, and acetamide, were identified during the EO processes. The most remarkable result of the present study is the demonstration of upcycling hazardous materials into valuable catalysts for the creation of electrodes to degrade hazardous water pollutants. Further investigations are intended to apply the current modulation technique, by continuously adjusting the applied current, to reduce the energy consumption, and develop topologically optimized flow-through electrodes, for developing a more efficient process.

References

Al-Gharibi, M.A., Kyaw, H.H., Al-Sabahi, J.N., Zar Myint, M.T., Al-Sharji, Z.A., Al-Abri, M.Z., 2021. Silver nanoparticles decorated zinc oxide nanorods supported catalyst for photocatalytic degradation of

paracetamol. Mater. Sci. Semicond. Process. 134, 105994. https://doi.org/10.1016/j.mssp.2021.105994
Anglada, A., Urtiaga, A., Ortiz, I., 2009. Contributions of electrochemical oxidation to waste-water treatment: fundamentals and review of applications. J. Chem. Technol. Biotechnol. 84, 1747–1755. https://doi.org/10.1002/jctb.2214
Araújo, K.C., dos Santos, E. V., Nidheesh, P. V., Martínez-Huitle, C.A., 2022. Fundamentals and advances on the mechanisms of electrochemical generation of persulfate and sulfate radicals in aqueous medium. Curr. Opin. Chem. Eng. 38, 100870. https://doi.org/10.1016/j.coche.2022.100870
Bepete, G., Voiry, D., Chhowalla, M., Chiguvare, Z., Coville, N.J., 2013. Incorporation of small BN domains in graphene during CVD using methane, boric acid and nitrogen gas. Nanoscale 5, 6552–6557. https://doi.org/10.1039/c3nr01699d
Brillas, E., 2021. Recent development of electrochemical advanced oxidation of herbicides. A review on its application to wastewater treatment and soil remediation. J. Clean. Prod. 290, 125841. https://doi.org/10.1016/j.jclepro.2021.125841
Brillas, E., Sirés, I., Arias, C., Cabot, P.L., Centellas, F., Rodríguez, R.M., Garrido, J.A., 2005. Mineralization of paracetamol in aqueous medium by anodic oxidation with a boron-doped diamond electrode. Chemosphere 58, 399–406. https://doi.org/10.1016/j.chemosphere.2004.09.028
Brito, L.R.D., Ganiyu, S.O., dos Santos, E. V., Oturan, M.A., Martínez-Huitle, C.A., 2021. Removal of antibiotic rifampicin from aqueous media by advanced electrochemical oxidation: Role of electrode materials, electrolytes and real water matrices. Electrochim. Acta 396, 139254. https://doi.org/10.1016/j.electacta.2021.139254
Cui, D., Yang, L.M., Liu, W.Z., Cui, M.H., Cai, W.W., Wang, A.J., 2018. Facile fabrication of carbon brush with reduced graphene oxide (rGO) for decreasing resistance and accelerating pollutants removal in bio-electrochemical systems. J. Hazard. Mater. 354, 244–249. https://doi.org/10.1016/j.jhazmat.2018.05.001
de Freitas Araújo, K.C., Vieira dos Santos, E., Pierpaoli, M., Ficek, M., Santos, J.E.L., Martínez-Huitle, C.A., Bogdanowicz, R., 2022. Diamondized carbon nanoarchitectures as electrocatalytic material for sulfate-based oxidizing species electrogeneration. Electrochim. Acta 430, 1–11. https://doi.org/10.1016/j.electacta.2022.141069
Del Corro, E., Taravillo, M., Baonza, V.G., 2014. Stress-dependent correlations for resonant Raman bands in graphite with defects. J. Raman Spectrosc. 45, 476–480. https://doi.org/10.1002/jrs.4475
Eckmann, A., Felten, A., Verzhbitskiy, I., Davey, R., Casiraghi, C., 2013. Raman study on defective graphene: Effect of the excitation energy, type, and amount of defects. Phys. Rev. B - Condens. Matter Mater. Phys. 88, 1–11. https://doi.org/10.1103/PhysRevB.88.035426
Environmental Protection Agency, 2014. Risk Assessment of Spent Foundry Sands In Soil-Related Applications Evaluating Silica-based Spent Foundry Sand From Iron, Steel, and Aluminum Foundries 477.
Faber, M.S., Dziedzic, R., Lukowski, M.A., Kaiser, N.S., Ding, Q., Jin, S., 2014. High-performance electrocatalysis using metallic cobalt pyrite (CoS 2) micro- and nanostructures. J. Am. Chem. Soc. 136, 10053–10061. https://doi.org/10.1021/ja504099w
Ganiyu, S.O.S.O., Martínez-Huitle, C.A.C.A., Oturan, M.A.M.A., 2021. Electrochemical advanced oxidation processes for wastewater treatment: Advances in formation and detection of reactive species and mechanisms. Curr. Opin. Electrochem. 27, 100678. https://doi.org/10.1016/j.coelec.2020.100678
Gharfalkar, M., Court, R., Campbell, C., Ali, Z., Hillier, G., 2015. Analysis of waste hierarchy in the European waste directive 2008/98/EC. Waste Manag. 39, 305–313.
Lee, J.E., Choi, J., Lee, D.J., Lee, S., Chae, H.G., 2022. Radial microstructure development of polyacrylonitrile (PAN)-based carbon fibers. Carbon N. Y. 191, 515–524. https://doi.org/10.1016/j.carbon.2022.02.023
Li, J., Ye, Q., Gan, J., 2014. Degradation and transformation products of acetaminophen in soil. Water Res. 49, 44–52. https://doi.org/10.1016/j.watres.2013.11.008

Martínez-Huitle, C.A., Panizza, M., 2018. Electrochemical oxidation of organic pollutants for wastewater treatment. Curr. Opin. Electrochem. 11, 62–71. https://doi.org/10.1016/j.coelec.2018.07.010

Martins Ferreira, E.H., Moutinho, M.V.O., Stavale, F., Lucchese, M.M., Capaz, R.B., Achete, C.A., Jorio, A., 2010. Evolution of the Raman spectra from single-, few-, and many-layer graphene with increasing disorder. Phys. Rev. B - Condens. Matter Mater. Phys. 82. https://doi.org/10.1103/PhysRevB.82.125429

Morales, D.M., Risch, M., 2021. Seven steps to reliable cyclic voltammetry measurements for the determination of double layer capacitance. JPhys Energy 3. https://doi.org/10.1088/2515-7655/abee33

Nematollahi, D., Shayani-Jam, H., Alimoradi, M., Niroomand, S., 2009. Electrochemical oxidation of acetaminophen in aqueous solutions: Kinetic evaluation of hydrolysis, hydroxylation and dimerization processes. Electrochim. Acta 54, 7407–7415. https://doi.org/10.1016/j.electacta.2009.07.077

Ormeno-Cano, N., Radjenovic, J., 2022. Electrochemical degradation of antibiotics using flow-through graphene sponge electrodes. J. Hazard. Mater. 431, 128462.

Pacheco-Álvarez, M., Picos Benítez, R., Rodríguez-Narváez, O.M., Brillas, E., Peralta-Hernández, J.M., 2022. A critical review on paracetamol removal from different aqueous matrices by Fenton and Fenton-based processes, and their combined methods. Chemosphere 303. https://doi.org/10.1016/j.chemosphere.2022.134883

Pierpaoli, M., Dettlaff, A., Szopińska, M., Karpienko, K., Wróbel, M., Łuczkiewicz, A., Fudala-Książek, S., Bogdanowicz, R., 2021a. Simultaneous opto-electrochemical monitoring of carbamazepine and its electro-oxidation by-products in wastewater. J. Hazard. Mater. 419. https://doi.org/10.1016/j.jhazmat.2021.126509

Pierpaoli, M., Jakóbczyk, P., Dec, B., Giosuè, C., Czerwińska, N., Lewkowicz, A., Ruello, M.L., Bogdanowicz, R., 2022. A novel hierarchically-porous diamondized polyacrylonitrile sponge-like electrodes for acetaminophen electrochemical detection. Electrochim. Acta 430, 1–11. https://doi.org/10.1016/j.electacta.2022.141083

Pierpaoli, M., Jakobczyk, P., Sawczak, M., Łuczkiewicz, A., Fudala-Książek, S., Bogdanowicz, R., 2021b. Carbon nanoarchitectures as high-performance electrodes for the electrochemical oxidation of landfill leachate. J. Hazard. Mater. 401, 123407. https://doi.org/10.1016/j.jhazmat.2020.123407

Pierpaoli, M., Rycewicz, M., Łuczkiewicz, A., Fudala-Książek, S., Bogdanowicz, R., Ruello, M.L., 2020. Electrodes criticality: the impact of CRMs in the leachate electrochemical oxidation. Manuf. Rev. 7, 7. https://doi.org/10.1051/mfreview/2020006

Pierpaoli, M., Szopińska, M., Wilk, B.K., Sobaszek, M., Łuczkiewicz, A., Bogdanowicz, R., Fudala-Książek, S., 2021c. Electrochemical oxidation of PFOA and PFOS in landfill leachates at low and highly boron-doped diamond electrodes. J. Hazard. Mater. 403. https://doi.org/10.1016/j.jhazmat.2020.123606

Rajabpour, S., Mao, Q., Gao, Z., Khajeh Talkhoncheh, M., Zhu, J., Schwab, Y., Kowalik, M., Li, X., van Duin, A.C.T., 2021. Low-temperature carbonization of polyacrylonitrile/graphene carbon fibers: A combined ReaxFF molecular dynamics and experimental study. Carbon N. Y. 174, 345–356. https://doi.org/10.1016/j.carbon.2020.12.038

Randles, J.E.B., 1947. Kinetics of rapid electrode reactions. Discuss. faraday Soc. 1, 11–19.

Santos, J.E.L., Gomez, M.A., de Moura, D.C., Cerro-López, M., Quiroz, M.A., Martínez-Huitle, C.A., 2021. Removal of herbicide 1-chloro-2, 4-dinitrobenzene (DNCB) from aqueous solutions by electrochemical oxidation using boron-doped diamond (BDD) and PbO2 electrodes. J. Hazard. Mater. 402, 123850.

Shestakova, M., Sillanpää, M., 2017. Electrode materials used for electrochemical oxidation of organic compounds in wastewater. Rev. Environ. Sci. Biotechnol. https://doi.org/10.1007/s11157-017-9426-1

Siddique, R., Singh, G., 2011. Utilization of waste foundry sand (WFS) in concrete manufacturing. Resour. Conserv. Recycl. 55, 885–892. https://doi.org/10.1016/j.resconrec.2011.05.001

Tian, W., Zhang, H., Duan, X., Sun, H., Shao, G., Wang, S., 2020. Porous carbons: Structure-oriented design and versatile applications. Adv. Funct. Mater. 30, 1909265.

Wang, P., Hu, Y., Cheng, H., 2019. Municipal solid waste (MSW) incineration fly ash as an important source of heavy metal pollution in China. Environ. Pollut. 252, 461–475.

Wilk, B.K., Szopińska, M., Sobaszek, M., Pierpaoli, M., Błaszczyk, A., Luczkiewicz, A., Fudala-Ksiazek, S., Krystyna, B., Malgorzata, W., Michał, S., Mattia, S., Agata, P., 2022. Electrochemical oxidation of landfill leachate using boron-doped diamond anodes: pollution degradation rate, energy efficiency and toxicity assessment. Environ. Sci. Pollut. Res. 1–17. https://doi.org/10.1007/s11356-022-19915-3

Wu, S., Zhang, L., Chen, J., 2012. Paracetamol in the environment and its degradation by microorganisms. Appl. Microbiol. Biotechnol. 96, 875–884. https://doi.org/10.1007/s00253-012-4414-4

Zhang, Q., Cao, Y., Yan, Y., Yuan, B., Zheng, H., Gu, Y., Zhong, X., Wang, J., 2020. Synergetic effect of pyrrolic-N and doped boron in mesoporous carbon for electrocatalytic ozone production. J. Mater. Chem. A 8, 2336–2342. https://doi.org/10.1039/c9ta12866b

Zhang, Q., Yang, Y.-L., Zhou, Y., Hong, J., 2022. Paracetamol degradation via electrocatalysis with B and N co-doped reduced graphene oxide: Insight into the mechanism on catalyst surface and in solution. Chemosphere 287, 132070.

Zhang, Y., Wang, B., Cagnetta, G., Duan, L., Yang, J., Deng, S., Huang, J., Wang, Y., Yu, G., 2018. Typical pharmaceuticals in major WWTPs in Beijing, China: Occurrence, load pattern and calculation reliability. Water Res. 140, 291–300. https://doi.org/10.1016/j.watres.2018.04.056